

Contents lists available at [ScienceDirect](#)

Journal of Quantitative Spectroscopy & Radiative Transfer

journal homepage: www.elsevier.com/locate/jqsrt

Radiation characteristics and effective optical properties of dumbbell-shaped cyanobacterium *Synechocystis* sp.



Ri-Liang Heng, Laurent Pilon*

Mechanical and Aerospace Engineering Department, Henry Samueli School of Engineering and Applied Science, University of California, 420 Westwood Plaza, Eng. IV 37-132, Los Angeles, CA 90095, USA

ARTICLE INFO

Article history:

Received 30 July 2015

Accepted 19 January 2016

Available online 25 January 2016

Keywords:

Radiative transfer

Scattering measurements

Turbid media

Inverse scattering

Optical constants

ABSTRACT

This study presents experimental measurements of the radiation characteristics of unicellular freshwater cyanobacterium *Synechocystis* sp. during their exponential growth in F medium. Their scattering phase function at 633 nm average spectral absorption and scattering cross-sections between 400 and 750 nm were measured. In addition, an inverse method was used for retrieving the spectral effective complex index of refraction of overlapping or touching bispheres and quadspheres from their absorption and scattering cross-sections. The inverse method combines a genetic algorithm and a forward model based on Lorenz–Mie theory, treating bispheres and quadspheres as projected area and volume-equivalent coated spheres. The inverse method was successfully validated with numerically predicted average absorption and scattering cross-sections of suspensions consisting of bispheres and quadspheres, with realistic size distributions, using the T-matrix method. It was able to retrieve the monomers' complex index of refraction with size parameter up to 11, relative refraction index less than 1.3, and absorption index less than 0.1. Then, the inverse method was applied to retrieve the effective spectral complex index of refraction of *Synechocystis* sp. approximated as randomly oriented aggregates consisting of two overlapping homogeneous spheres. Both the measured absorption cross-section and the retrieved absorption index featured peaks at 435 and 676 nm corresponding to chlorophyll *a*, a peak at 625 nm corresponding to phycocyanin, and a shoulder around 485 nm corresponding to carotenoids. These results can be used to optimize and control light transfer in photobioreactors. The inverse method and the equivalent coated sphere model could be applied to other optically soft particles of similar morphologies.

© 2016 Elsevier Ltd. All rights reserved.

1. Introduction

Photosynthetic microorganisms use sunlight as their energy source and carbon dioxide as their carbon source. They can be cultivated to produce a variety of valuable products such as nutritional supplements, natural dyes,

cosmetics, biofuels, and fertilizers [1,2]. In addition, they can be used to treat wastewater [2] and to reduce carbon dioxide emissions from industrial exhaust gases [3]. However, key advances in cultivation systems and biomass harvesting methods are required to improve productivity and make the technology cost effective [4].

The unicellular freshwater cyanobacterium *Synechocystis* sp. PCC 6803 has been considered for biofuel production [5]. It was the first photosynthetic organism whose entire genome was sequenced due to the

* Corresponding author. Tel.: +1 310 206 5598; fax: +1 310 206 2302.
E-mail address: pilon@seas.ucla.edu (L. Pilon).

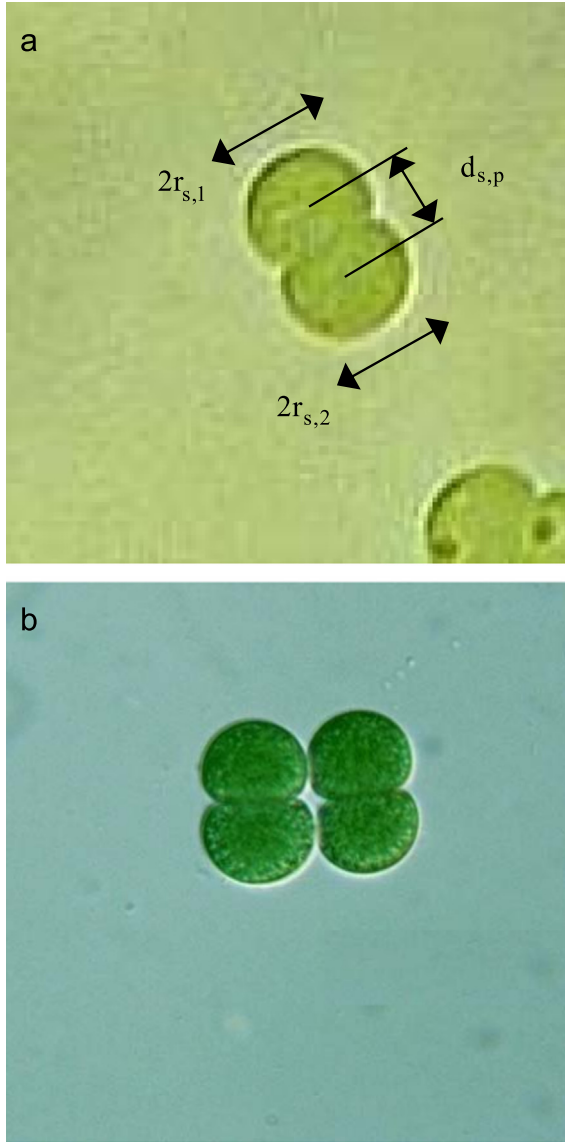


Fig. 1. Micrographs of (a) a free floating dumbbell-shaped *Synechocystis* sp. cell with two lobes of radius $r_{s,1}$ and $r_{s,2}$ of about $1\ \mu\text{m}$ and (b) *Synechocystis* sp. immediately after cell division. Reproduced with permission from Prof. Yuuji Tsukii (Hosei University, <http://protist.i.hosei.ac.jp/>).

similarities between its photosynthetic apparatus and that of higher plants [6]. It is widely used as a standard in studies involving photosynthesis, environmental stress response, pigment synthesis, lipid production, and other metabolic processes [6–9]. *Synechocystis* sp. contain different photosynthetic pigments including Chlorophyll *a* (Chl *a*), phycocyanin (PCCN), as well as photosynthetic (PSC) and photoprotective (PPC) carotenoids [10]. Each type of pigments possesses its own absorption spectra enabling the microorganisms to absorb photons in the photosynthetically active radiation (PAR) region ranging from 400 to 700 nm [11]. This species has also been genetically engineered with reduced light harvesting pigments (particularly PCCN), to increase their energetic yield

per cell [5]. Fig. 1a shows a micrograph of dumbbell-shaped *Synechocystis* sp. cells approximately $2\ \mu\text{m}$ in length and resembling overlapping bispheres. Fig. 1b shows a micrograph of *Synechocystis* sp. immediately after fission when the cell divides into two identical daughter cells and resembling quadraspheres [12].

Photosynthetic microorganisms are typically cultivated in open or closed photobioreactor (PBR) systems. The productivity of these systems is severely hampered by low light energy conversion efficiencies [13]. Indeed, incident light is rapidly attenuated in the culture due to light absorption and scattering by the microorganisms, resulting in inhomogeneous light distribution. In regions of the PBRs directly exposed to sunlight, the light intensity may be excessively high causing photoinhibition [14]. On the other hand, deeper in the PBR, light intensity may be too small to drive photosynthesis or even respiration. Both phenomena result in low photosynthetic efficiency and in a significant decrease in the overall PBR productivity. Therefore, PBR design and control must be improved so that light can be utilized as efficiently as possible. In order to do so, analytical tools modeling coupled light transfer, hydrodynamics, and growth kinetics have been developed [15–17]. In all these models, the spectral radiation characteristics of the photosynthetic microorganisms are essential input parameters.

The present study aims to measure the radiation characteristics of *Synechocystis* sp. during exponential growth. It also aims to develop an inverse method able to retrieve the effective spectral complex index of refraction of *Synechocystis* sp. and other particles with complex touching or overlapping bisphere and quadrasphere morphologies from their absorption and scattering cross-sections.

2. Background

2.1. Light transfer

The spectral radiation intensity $I_\lambda(r, \hat{\mathbf{s}})$ (in $\text{W}/\text{m}^2\ \text{sr}\ \text{nm}$) along the direction $\hat{\mathbf{s}}$ at location \mathbf{r} and wavelength λ in homogeneous, absorbing, scattering, and non-emitting microorganism suspensions satisfies the radiative transfer equation (RTE) expressed as [18]

$$\hat{\mathbf{s}} \cdot \nabla I_\lambda(\mathbf{r}, \hat{\mathbf{s}}) = -\kappa_\lambda I_\lambda(\mathbf{r}, \hat{\mathbf{s}}) - \sigma_{s,\lambda} I_\lambda(\mathbf{r}, \hat{\mathbf{s}}) + \frac{\sigma_{s,\lambda}}{4\pi} \int_{4\pi} I_\lambda(\mathbf{r}, \hat{\mathbf{s}}_i) \Phi_{T,\lambda}(\hat{\mathbf{s}}_i, \hat{\mathbf{s}}) d\Omega_i \quad (1)$$

where κ_λ and $\sigma_{s,\lambda}$ are the effective spectral absorption and scattering coefficients of the suspension (in m^{-1}), respectively. In addition, the extinction coefficient is defined as $\beta_\lambda = \kappa_\lambda + \sigma_{s,\lambda}$. The scattering phase function $\Phi_{T,\lambda}(\hat{\mathbf{s}}_i, \hat{\mathbf{s}})$ represents the probability that light propagating in the solid angle $d\Omega_i$ along direction $\hat{\mathbf{s}}_i$ be scattered into the solid angle $d\Omega$ along direction $\hat{\mathbf{s}}$. It is normalized such that

$$\frac{1}{4\pi} \int_{4\pi} \Phi_{T,\lambda}(\hat{\mathbf{s}}_i, \hat{\mathbf{s}}) d\Omega_i = 1. \quad (2)$$

In addition, the asymmetry factor g_λ for an axisymmetric

phase function is defined as [18]

$$g_\lambda = \frac{1}{2} \int_0^\pi \Phi_{T,\lambda}(\theta) \cos \theta \sin \theta d\theta \quad (3)$$

where θ is the scattering angle between directions \hat{s}_i and \hat{s} .

The average absorption $\bar{C}_{abs,\lambda}$ and scattering $\bar{C}_{sca,\lambda}$ cross-sections (in m^2) of a suspension of polydisperse microorganism cells can be related to the spectral absorption κ_λ and scattering $\sigma_{s,\lambda}$ coefficients according to [18]

$$\bar{C}_{abs,\lambda} = \frac{\kappa_\lambda}{N_T} \quad \text{and} \quad \bar{C}_{sca,\lambda} = \frac{\sigma_{s,\lambda}}{N_T} \quad (4)$$

where N_T is the cell number density defined as the number of cells per m^3 of suspension.

2.2. Radiation characteristics of photosynthetic microorganisms

The absorption and scattering cross-sections and the scattering phase function of photosynthetic microorganisms in the PAR region depend on wavelength as well as on their morphologies, size, and composition. They can be determined either experimentally or numerically. Previous experimental studies have focused on randomly oriented quasi-spherical microalgae [18,19] and filamentous cyanobacteria [20,21]. However, the experimental method previously used by Pilon and co-workers [21–23] for various microalgae and cyanobacteria species is not limited to any specific shape and can also be used for *Synechocystis* sp., as discussed later in this paper.

Numerical predictions of the radiation characteristics of photosynthetic microorganisms have typically treated them as homogeneous spheres [19,24–31]. They predicted their radiation characteristics based on their size distribution and a model or experimental estimate of their effective complex index of refraction. Then, their radiation characteristics can be calculated using fast analytical solutions such as the Lorenz–Mie theory [32] or the anomalous diffraction approximation [33]. Numerical methods, such as the T-matrix method [34], can also compute the radiation characteristics of scatterers with complex shapes such as (i) unicellular photosynthetic microorganisms with non-spherical shapes (e.g., spheroidal [35] and bisphere [36]), (ii) multicellular microorganisms (e.g., filamentous cyanobacteria [21]), and (iii) fractal colonies of unicellular spherical microalgae [37]. However, these methods can be time-consuming, computationally intensive, and limited to a certain range of size parameters [36]. Alternatively, photosynthetic microorganisms of complex morphology, including many cyanobacteria, could be treated as equivalent scattering particles with simpler shape including infinitely long cylinders and coated spheres [24,25,31,35,36] whose radiation characteristics can be computed relatively simply [38–40]. For example, Lee and Pilon [41] reported that randomly oriented filamentous cyanobacteria consisting of linear chains of optically soft spheres could be modeled as randomly oriented volume-equivalent infinitely long cylinders for the purpose of predicting their integral radiation characteristics, namely κ_λ , $\sigma_{s,\lambda}$, and g_λ . Similarly, Heng

et al. [36] demonstrated that the integral radiation characteristics of randomly oriented multicellular cyanobacteria with morphologies of bispheres, quadspheres, and rings of spheres could be approximated as those of equivalent coated spheres with identical volume and average projected area. Kandilian et al. [37] demonstrated that this approximation was also valid for randomly oriented fractal colonies of spherical unicellular microalgae. This approximation leads to significant savings in computational time and resources compared with numerical predictions using the T-matrix method.

Regardless of the numerical method or approximate formulation, the effective complex index of refraction of microorganisms is essential to compute the radiation characteristics. Although the cells were actually heterogeneous in nature, most studies have treated photosynthetic microorganisms as homogeneous spheres with some effective optical properties [19,24–31,35–37,41]. Aas [28] estimated the effective refractive index (real part) of phytoplankton cells from their metabolite composition by using a volume-weighted average of the refractive indices of the various constituents including proteins, carbohydrates, water, and lipids. Pottier et al. [29] predicted the spectral absorption index (imaginary part) of *Chlamydomonas reinhardtii* as a weighted sum of the absorption indices of the major algal pigments and assumed their refractive index to be constant and equal to 1.527. More recently, Dauchet [42] used the same method as Pottier et al. [29] to estimate k_λ but predicted n_λ , on a spectral basis, using subtractive Kramers–Kronig relationship relating n_λ to k_λ .

Alternatively, the effective complex index of refraction of microorganisms has been retrieved from experimental measurements of their absorption and scattering cross-sections using inverse methods [21,26,31,43]. Here also, treating the microorganism cells as simple equivalent scattering particles, in order to compute their radiation characteristics, is essential since the forward problem has to be solved numerous times. For example, Bricaud and Morel [26] predicted the effective complex index of refraction of phytoplanktonic cells by treating them as homogeneous spheres, based on the anomalous diffraction approximation. The absorption coefficient was described as a continuous and monotonic function of the effective absorption index for given wavelength and particle size distribution. Then, the spectral absorption index of the cells was determined by iteration until the computed spectral absorption coefficient agreed with the experimentally measured value. The retrieved refractive and absorption indices were used as input parameters into the Lorenz–Mie theory. Subsequently, the spectral refractive index of the cells was obtained by iteration until the computed spectral extinction coefficient matched the experimentally measured value. On the other hand, Lee et al. [31] developed an inverse method combining genetic algorithm (GA) [44] and the Lorenz–Mie theory [32] to retrieve simultaneously the refractive and absorption indices of various quasi-spherical microalgae. Similarly, Heng et al. [21] combined GA with electromagnetic wave theory for randomly oriented and infinitely long cylinders [45,46] to retrieve the effective complex index of refraction

of filamentous cyanobacteria *Anabaena cylindrica* from their experimentally measured absorption and scattering cross-sections.

The objective of the present study is to experimentally measure the absorption $\bar{C}_{abs,\lambda}$ and scattering $\bar{C}_{sca,\lambda}$ cross-sections as well as the phase function $\Phi_{T,\lambda}(\hat{\mathbf{s}}_i, \hat{\mathbf{s}})$ of randomly oriented *Synechocystis* sp. under exponential growth. It also aims to develop an inverse method to retrieve the effective spectral complex index of refraction of photosynthetic microorganisms with complex bisphere and quadisphere shapes. The feasibility of the inverse method was demonstrated using numerically predicted absorption and scattering cross-sections of polydisperse bispheres and quadispheres obtained by the T-matrix method for different cell size distributions and complex index of refraction. Then, it was applied to the measured absorption and scattering cross-sections and size distribution of *Synechocystis* sp. cells approximated as two overlapping and homogeneous spherical monomers.

3. Experimental methods

3.1. Cultivation and sample preparation

The unicellular cyanobacterium *Synechocystis* sp. PCC 6803 was cultivated in F medium [47] in 250 ml culture bottles fitted with vented caps and illuminated from one side by a continuous photosynthetic photon flux density of $91 \mu\text{mol}_{hv} \text{m}^{-2} \text{s}^{-1}$ provided by fluorescent light bulbs (GroLux by Sylvania, USA). The culture was maintained at 30°C throughout the growth and the cell number density N_T (in $/\text{m}^3$) was measured daily using an automatic cell counter (Nexcelom Cellometer Auto M10). To do so, 20 μL samples were pipetted from the cultures into disposable haemocytometers (Nexcelom CHT4-SD100). The device counted the number of cells per unit volume N_T using 2D micrographs. Prior to taking a sample, the culture was shaken manually to ensure that it was well-mixed and that the sample was representative of the entire culture volume.

Six days after inoculation, the cultures were observed to be in their exponential growth phase based on cell density measurements. Then, the suspension was thoroughly shaken and samples of 3 ml were collected to measure their radiation characteristic measurements. To prevent possible absorption and scattering by F medium, the samples were centrifuged at 2000 rpm (1300 g) for 8 min. Then, the supernatant was replaced with non-absorbing phosphate buffer saline (PBS) solution and the samples were lightly vortexed to resuspend the *Synechocystis* sp. cells.

3.2. Size distribution

In order to characterize the size distribution of *Synechocystis* sp., micrographs of the cells were captured using a $100\times$ Leica inverted microscope connected to a CCD camera. We considered $N_{sp}=252$ cells and manually measured (i) the radii $r_{s,1}$ and $r_{s,2}$ of the two lobes in each cell and (ii) the distance d_{sp} separating the lobes' centers

using the image analysis software ImageJ, as illustrated in Fig. 1a. Only the cells whose dumbbell shape could be easily discerned were selected for measurements. The morphology of the cells was simplified to that of bispheres consisting of two identical overlapping spherical monomers of radius $r_s = (r_{s,1} + r_{s,2})/2$ (Fig. 3a). These measurements led to the frequency distributions $f_{b,exp}(r_s)$ and $f_{d,exp}(d_{sp})$ of the bisphere approximating *Synechocystis* sp.

3.3. Radiation characteristics measurements

The following assumptions were made in measuring the scattering phase function and the average spectral absorption and scattering cross-sections of *Synechocystis* sp.: (1) the suspension in the samples were well mixed and the cells were randomly oriented. Thus, the suspension had azimuthally symmetric phase function depending only on polar angle θ . (2) Single scattering prevailed due to the low cell number densities considered. (3) The scattering phase function of *Synechocystis* sp. cells was assumed to be constant over the PAR region [22], and (4) largely forward scattering because of their large size parameters in the PAR region.

The experimental setup, data analysis, and validation with latex microspheres were reported in detail by Pilon and co-workers [18,20,22,48] and need not be repeated. In brief, the scattering phase function $\Phi_{T,\lambda}(\theta)$ of the *Synechocystis* sp. suspension was measured with a polar nephelometer equipped with a laser at 633 nm. Due to obstruction by the probe, the scattering phase function for scattering angles θ beyond 160° in the backward direction was not reported. Normal-normal transmittance of the microorganism suspension, denoted by $T_{n,\lambda}$, was measured in cuvettes of pathlength $l=1$ cm using a UV-VIS spectrophotometer (Shimadzu, USA, Model UV-3103PC) from 400 to 750 nm with 1 nm spectral resolution [48]. These measurements were calibrated using the transmittance of the reference medium (i.e., PBS), denoted by $T_{n,\lambda,ref}$, in order to correct for reflection and refraction by the cuvette. These measurements were used to determine the extinction coefficient β_λ of the suspension. The data analysis corrected for the fact that a fraction of the light scattered in the forward direction was captured by the detector due to its finite acceptance angle. Similarly, normal-hemispherical transmittance $T_{h,\lambda}$ was measured with an integrating sphere (ISR-3100 by Shimadzu, USA) and the above-mentioned spectrophotometer. Here also, the measurements were calibrated with the normal-hemispherical transmittance of the reference medium $T_{h,\lambda,ref}$. They were used to determine the absorption coefficient κ_λ of the suspension. The data analysis corrected for imperfect reflections in the inner surface of the integrating sphere and the geometry of the setup resulting in a fraction of the scattered and transmitted light being unable to reach the detector.

Prior to all transmission measurements, the samples were manually shaken to ensure a well-mixed suspension with randomly oriented *Synechocystis* sp. cells. In addition, the measurements were performed for two different cell number densities by diluting the samples with PBS. For each sample, the normal-normal and normal-

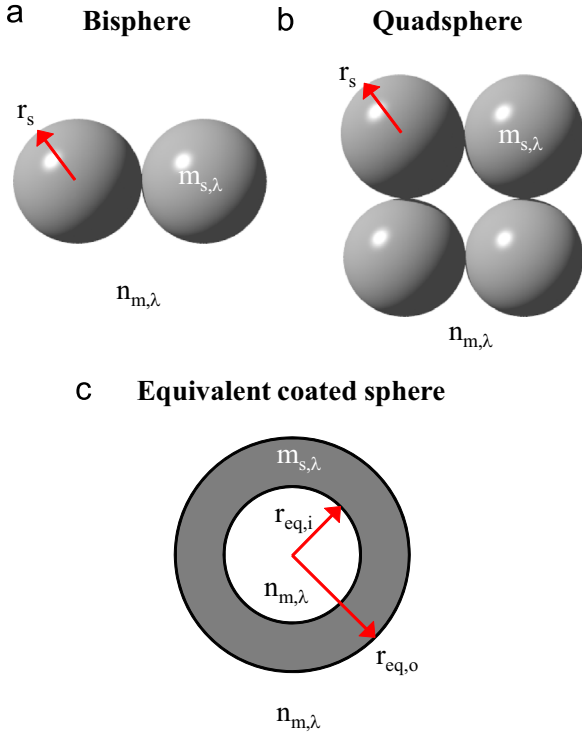


Fig. 2. Schematics of (a) a bisphere, (b) a quadisphere, and (c) an average projected area and volume-equivalent coated sphere with inner radius $r_{eq,i}$ and outer radius $r_{eq,o}$. The monomers and the coating of the coated sphere had the same complex index of refraction $m_{s,\lambda}$. The surrounding medium and the core of the coated sphere were non-absorbing with refractive index $n_{m,\lambda}$.

hemispherical transmittances were measured three times and the results were averaged. Absorption κ_λ and scattering $\sigma_{s,\lambda}$ coefficients were normalized by the measured cell number density N_T according to Eq. (4) to obtain the average absorption $\bar{C}_{abs,\lambda}$ and scattering $\bar{C}_{sca,\lambda}$ cross-sections of the microorganisms. It was established that single and independent scattering prevailed by verifying that the cross-sections $\bar{C}_{abs,\lambda}$ and $\bar{C}_{sca,\lambda}$ for different values of cell densities N_T collapsed onto a single line [33].

Finally, note that radiation characteristics of microorganisms may vary with time in response to changes in light and nutrient availability [23,48]. However, it was established that light transfer in PBRs can be accurately predicted throughout the PBR operation, except under nutrient limitations, based on the radiation characteristics measured during the exponential growth phase [48].

4. Analysis

4.1. Aggregates and their equivalent coated spheres

Figs. 2a and 2b show schematics of a bisphere and a quadisphere, respectively. The number of spherical monomers in each aggregate was denoted by N_s , e.g., $N_s=2$ for bispheres and $N_s=4$ for quadispheres. In addition, the radius of the monomers was denoted by r_s and the monomer size parameter was defined as $\chi_s = 2\pi r_s/\lambda$. The

monomers had effective spectral complex index of refraction $m_{s,\lambda} = n_{s,\lambda} + ik_{s,\lambda}$ where $n_{s,\lambda}$ and $k_{s,\lambda}$ denote the spectral refractive and absorption indices, respectively. The surrounding medium was non-absorbing and had spectral refractive index $n_{m,\lambda}$. Then, the relative refractive n_λ and absorption k_λ indices of the monomers can be defined as

$$n_\lambda = \frac{n_{s,\lambda}}{n_{m,\lambda}} \quad \text{and} \quad k_\lambda = \frac{k_{s,\lambda}}{n_{m,\lambda}}. \quad (5)$$

Fig. 2c shows a schematic of the average projected area and volume-equivalent coated sphere whose coating has the same complex index of refraction $m_{s,\lambda}$ as the monomers while its core consists of the surrounding medium of refractive index $n_{m,\lambda}$. Its equivalent inner $r_{eq,i}$ and outer $r_{eq,o}$ radii are expressed as [36]

$$r_{eq,i} = \sqrt[3]{\left(\frac{\bar{A}_p}{\pi}\right)^{3/2} - \frac{3V}{4\pi}} \quad \text{and} \quad r_{eq,o} = \sqrt{\frac{\bar{A}_p}{\pi}} \quad (6)$$

where V and \bar{A}_p are the volume and average projected area of the monomer aggregates, respectively. In particular, the volume of bisphere V_b and of quadisphere V_q can be expressed as

$$V_{b/q} = \frac{4}{3}\pi N_s r_s^3. \quad (7)$$

The average projected area of bispheres $\bar{A}_{p,b}$ and quadispheres $\bar{A}_{p,q}$ can be computed numerically and have been related to the monomer radius r_s according to [36]

$$\bar{A}_{p,b} = 5.35r_s^2 \quad \text{and} \quad \bar{A}_{p,q} = 9.70r_s^2. \quad (8)$$

Fig. 3a shows a schematic of two overlapping spheres of radius r_s whose centers are separated by a distance d_{sp} such that $r_s \leq d_{sp} \leq 2r_s$. This morphology is analogous to actual *Synechocystis* cells (Fig. 1). Its volume can be expressed as [49]

$$V_{syn} = \frac{8}{3}\pi r_s^3 - \frac{\pi}{12}(4r_s + d_{sp})(2r_s - d_{sp})^2 \quad (9)$$

Fig. 3b shows the ratio of the computed average projected area $\bar{A}_{p,syn}$ of randomly oriented overlapping bispheres to the projected area πr_s^2 of a monomer as a function of $d_{sp}/2r_s$ for different monomer radius r_s ranging from 1 to 9 μm . The results were obtained using the numerical method described in Ref. [36]. It is interesting to note that the plots of $\bar{A}_{p,syn}/\pi r_s^2$ vs. $d_{sp}/2r_s$ collapsed on a single line for all values of r_s considered. Least square fitting of the data yielded

$$\frac{\bar{A}_{p,syn}}{\pi r_s^2} = 1 + 0.872\left(\frac{d_{sp}}{2r_s}\right) - 0.169\left(\frac{d_{sp}}{2r_s}\right)^2 \quad (10)$$

Note that the expression $\bar{A}_{p,syn}$ gives the projected area of (i) a single sphere when $d_{sp} = 0 \mu\text{m}$ and (ii) $\bar{A}_{p,b}$ given by Eq. (8) for bispheres when $d_{sp} = 2r_s$. Also, the average projected area of *Synechocystis* can be measured from two-dimensional micrographs of randomly oriented cells [50].

4.2. Inverse method algorithm

4.2.1. Methodology

Fig. 4 shows the block diagram of the inverse method used to retrieve the refractive $n_{s,\lambda}$ and absorption $k_{s,\lambda}$

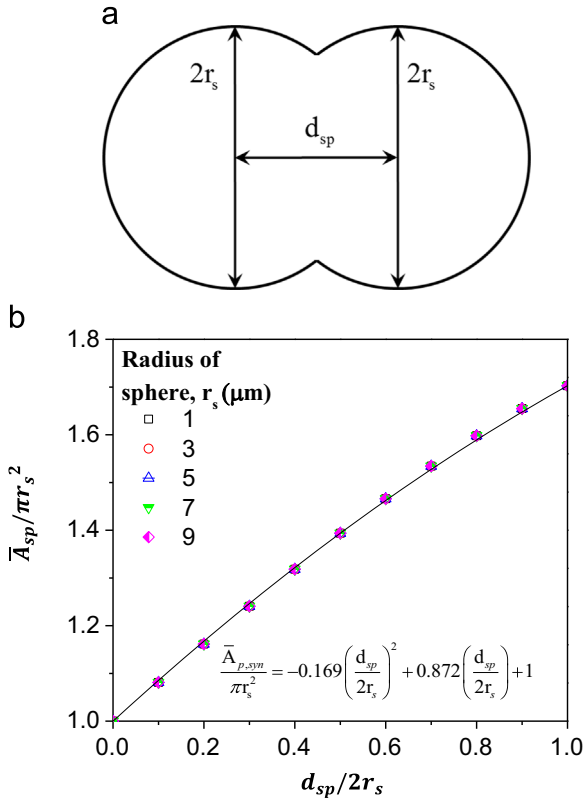


Fig. 3. (a) Schematic of overlapping spheres of radius r_s whose centers are separated by a distance d_{sp} , (b) ratio of the average projected area $\bar{A}_{p,sp}$ and the project area πr_s^2 of a single sphere as a function of $d_{sp}/2r_s$ for different values of r_s .

indices of the monomers of polydisperse bispheres and quadspheres at each wavelength λ from (i) the spectral refractive index $n_{m,\lambda}$ of the medium, (ii) the equivalent coated sphere radii distributions $f_i(r_{eq,i})$ and $f_o(r_{eq,o})$, and (iii) the measured average spectral absorption $\bar{C}_{abs,\lambda}$ and (iv) scattering $\bar{C}_{sca,\lambda}$ cross-sections. The Lorenz–Mie theory for coated spheres [38,46] was used in the forward model to calculate the predicted average absorption $\bar{C}_{abs,\lambda,pred}$ and scattering $\bar{C}_{sca,\lambda,pred}$ cross-sections. Then, the general purpose genetic algorithm PIKAIA [44] was used to simultaneously retrieve the values of $(n_{s,\lambda}, k_{s,\lambda})$ or (n_λ, k_λ) that minimized the difference between the measured average absorption $\bar{C}_{abs,\lambda}$ and scattering $\bar{C}_{sca,\lambda}$ cross-sections of the aggregates and those predicted using the equivalent coated sphere approximation $\bar{C}_{abs,\lambda,pred}$ and $\bar{C}_{sca,\lambda,pred}$. The choice of genetic algorithm was arbitrary and other optimization methods could have been used. However, it provides a reliable method for minimizing the objective function δ_λ defined, at each wavelength λ , as

$$\delta_\lambda = \left(\frac{\bar{C}_{abs,\lambda,pred} - \bar{C}_{abs,\lambda}}{\bar{C}_{abs,\lambda}} \right)^2 + \left(\frac{\bar{C}_{sca,\lambda,pred} - \bar{C}_{sca,\lambda}}{\bar{C}_{sca,\lambda}} \right)^2. \quad (11)$$

The genetic algorithm used a maximum of 500 generations and a population of 100 individuals per generation. Each individual consists of a pair $(n_{s,\lambda}, k_{s,\lambda})$. In the case when a generation featured an individual producing a value of δ_λ smaller than 10^{-4} , the corresponding values of $n_{s,\lambda}$ and $k_{s,\lambda}$ were reported as the retrieved refractive and absorption indices of the monomer at wavelength λ . Then, this procedure was repeated for another wavelength. The inverse method was implemented on a single dual core 2.53 GHz CPU with 4.00 GB RAM.

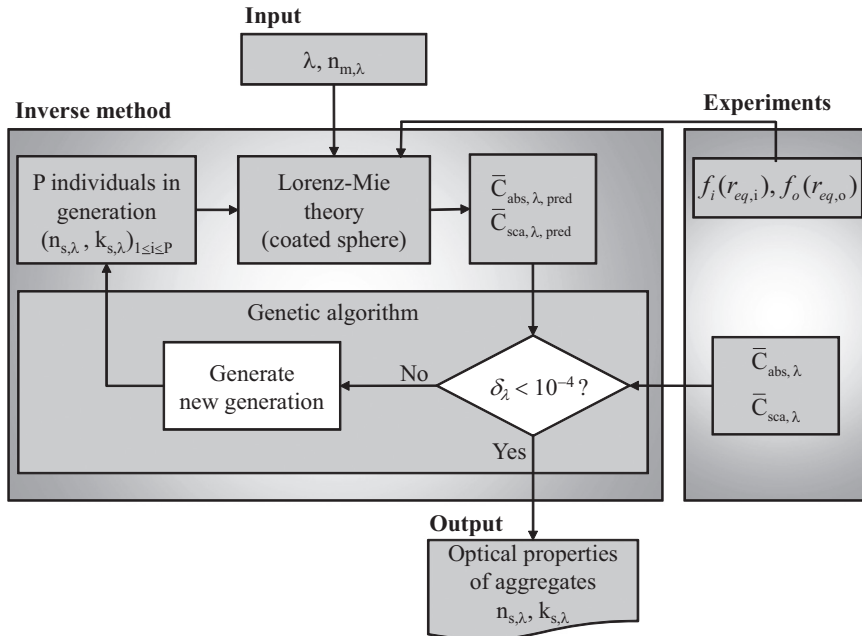


Fig. 4. Block diagram of the procedure used to retrieve the refractive index $n_{s,\lambda}$ and absorption index $k_{s,\lambda}$ from the measured average spectral absorption and scattering cross-sections $\bar{C}_{abs,\lambda}$ and $\bar{C}_{sca,\lambda}$ and the volume and average projected area equivalent coated sphere radii distribution $f(r_{eq,i}, r_{eq,o})$. Here, $P=100$ individuals per generation for a maximum of 500 generations. The objective function δ_λ to be minimized for each wavelength is defined in Eq. (11).

4.2.2. Validation

In order to assess the validity of the inverse method for a broad range of suspensions and monomer relative complex index of refraction $m_\lambda = n_\lambda + ik_\lambda$, we considered two different suspensions of bispheres and quadrspheres with various size distributions. The average absorption $\bar{C}_{abs,\lambda}$ and scattering $\bar{C}_{sca,\lambda}$ cross-sections of these suspensions were computed using the T-matrix method [34]. These results were then used in the inverse method to retrieve the relative refractive and absorption indices denoted by $n_{\lambda,pred}$ and $k_{\lambda,pred}$, respectively.

Suspension 1 consisted of $N_b=1000$ bispheres composed of two identical spherical monomers of radius frequency distribution $f_b(r_s)$. Suspension 2 was a mixture of aggregates consisting of $N_b=1000$ bispheres from Suspension 1 and $N_q=200$ quadrspheres with monodisperse spherical monomers of radius frequency distribution $f_q(r_s)$. The values of N_b and N_q were chosen arbitrarily as an upper estimate of the number of *Synechocystis* sp. cells undergoing cell division. In practice, only a few dividing cells could be observed at any given time under a microscope. Fig. 5a and b shows the histograms of the monomer radius frequency distributions $f_b(r_s)$ and $f_q(r_s)$ used for the bispheres and quadrspheres, respectively. These distributions were constructed using random

numbers generated by Matlab from a normal distribution with specified mean and standard deviation such that the largest size parameter did not exceed 10, corresponding to the upper limit for using the T-matrix code. They were then converted into the equivalent coated sphere radii frequency distributions $f_{1,i}(r_{eq,i}), f_{1,o}(r_{eq,o})$ and $f_{2,i}(r_{eq,i}), f_{2,o}(r_{eq,o})$, using Eqs. (6) and (8), as shown in Fig. 5c and d for Suspensions 1 and 2, respectively. The wavelength of the incident light was taken as constant and equal to 676 nm, corresponding to the in vivo absorption peak of Chl *a* [11]. This resulted in monomer size parameters χ_s of the bispheres and quadrspheres ranging from 5 to 11. In addition, the monomers were assigned a relative refractive index n_λ ranging from 1.03 to 2.0 and a relative absorption index k_λ ranging from 0.004 to 2.0.

For each combination of n_λ and k_λ , the absorption $C_{abs,i,j}$ and scattering $C_{sca,i,j}$ cross-sections of an individual randomly oriented bisphere or quadrsphere “j” were computed using the T-matrix method [34]. The average absorption $\bar{C}_{abs,\lambda}$ and scattering $\bar{C}_{sca,\lambda}$ cross-sections of the entire suspension were defined as

$$\bar{C}_{abs/sca,\lambda} = \frac{1}{N} \sum_{j=1}^N C_{abs/sca,\lambda,j}. \tag{12}$$

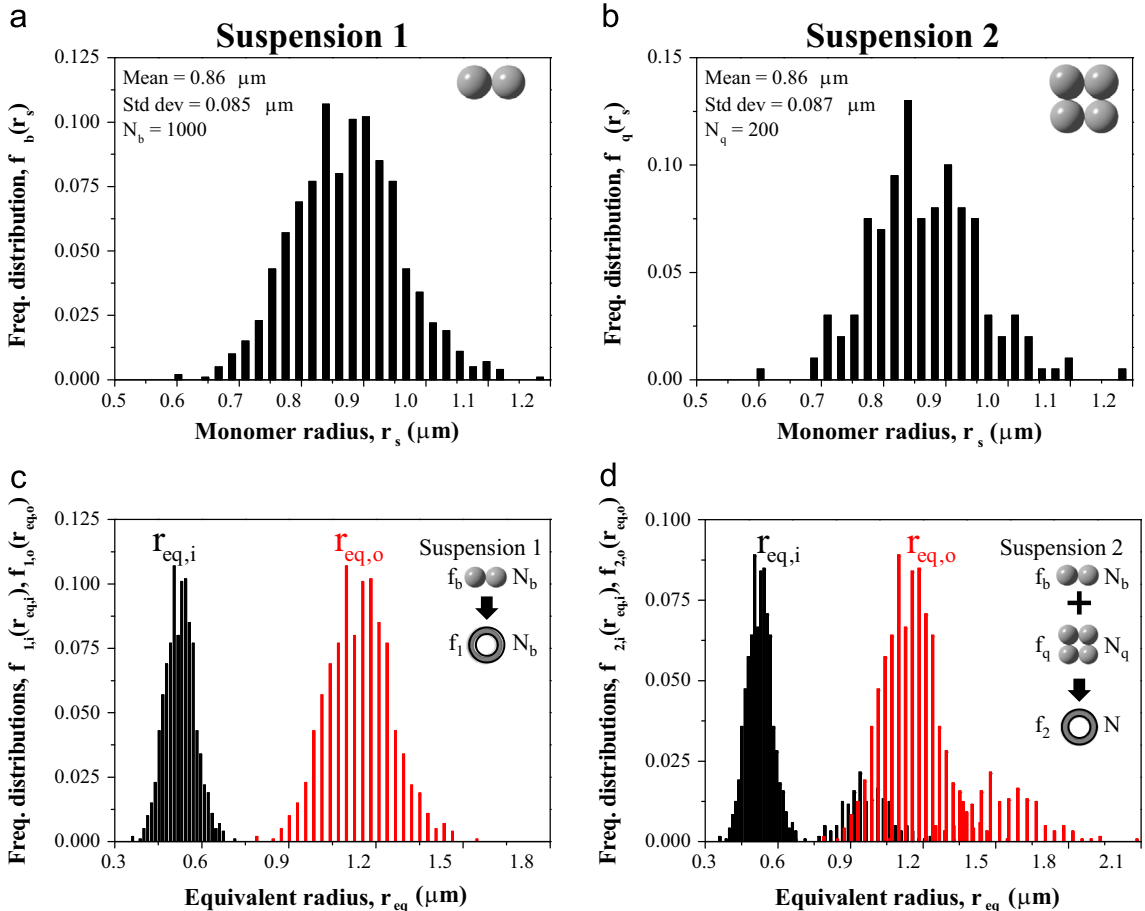


Fig. 5. Histograms of the bisphere and quadrsphere monomer radius frequency distribution and the equivalent coated sphere radii frequency distributions of Suspensions 1 and 2, respectively.

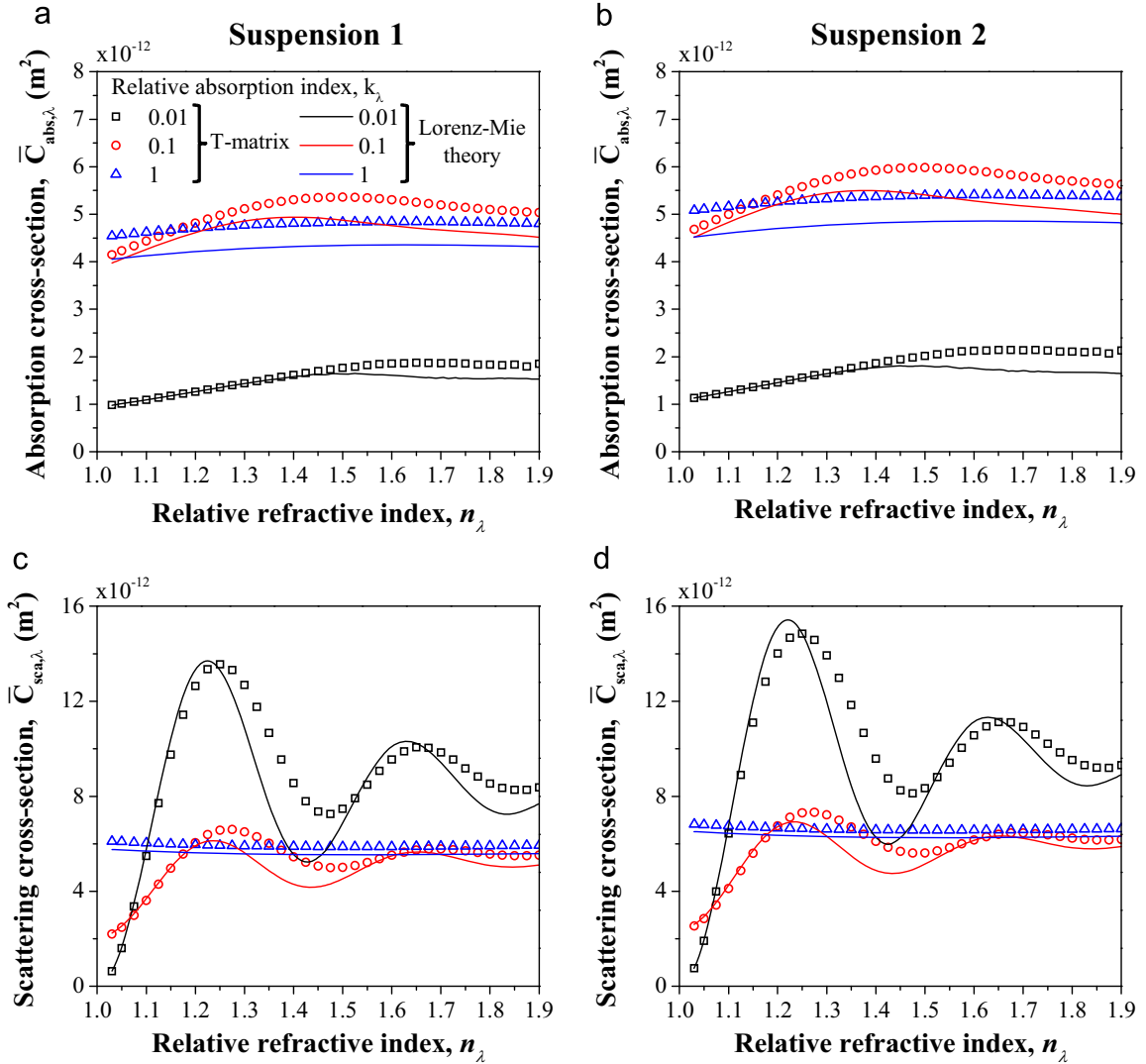


Fig. 6. (a, b) Average absorption $\bar{C}_{abs,\lambda}$ and (c, d) scattering $\bar{C}_{sca,\lambda}$ cross-sections predicted using the T-matrix method and the Lorenz–Mie theory for the corresponding equivalent coated spheres, as functions of relative refractive index n_λ ranging from 1.0 to 1.9 for relative absorption index $k_\lambda = 0.01, 0.1,$ and 1 for Suspensions 1 and 2, respectively.

where N is the total number of cells in the suspension, i.e., $N = N_b$ for Suspension 1 and $N = N_b + N_q$ for Suspension 2.

Finally, the equivalent coated sphere radii frequency distributions $f_{1/2,i}(r_{eq,i})$ and $f_{1/2,o}(r_{eq,o})$ for suspensions 1 or 2 and their average absorption $\bar{C}_{abs,\lambda}$ and scattering $\bar{C}_{sca,\lambda}$ cross-sections were used in conjunction with the inverse method to retrieve the relative refractive and absorption indices. These retrieved values $n_{\lambda,pred}$ and $k_{\lambda,pred}$ were compared with the values originally assigned to the monomers based on the sum of their absolute relative errors defined as

$$\epsilon_\lambda = \left| \frac{n_{\lambda,pred} - n_\lambda}{n_\lambda} \right| + \left| \frac{k_{\lambda,pred} - k_\lambda}{k_\lambda} \right|. \quad (13)$$

Figs. 6a and 6b plot the average absorption cross-sections $\bar{C}_{abs,\lambda}$ as a function of the relative refractive index n_λ for absorption index k_λ equal to 0.01, 0.1, and 1 for Suspensions 1 and 2, consisting of bispheres and of

bispheres and quadspheres, respectively. Similarly, Figs. 6c and 6d show the average scattering cross-sections $\bar{C}_{sca,\lambda}$ of Suspensions 1 and 2, respectively. These figures compare the cross-sections predicted by the T-matrix method with those corresponding to the average projected area and volume-equivalent coated spheres computed using the Lorenz–Mie theory and the size distributions $f_{1,i}(r_{eq,i})$, $f_{1,o}(r_{eq,o})$, $f_{2,i}(r_{eq,i})$, and $f_{2,o}(r_{eq,o})$. Fig. 6 indicates that, for given n_λ and k_λ , Suspension 2 had slightly larger $\bar{C}_{abs,\lambda}$ and $\bar{C}_{sca,\lambda}$ than Suspension 1 due to the fact that quadspheres were larger than bispheres and were responsible for additional absorption and scattering. It was also evident that $\bar{C}_{abs,\lambda}$ increased as k_λ increased from 0.01 to 0.1. However, when k_λ increased from 0.1 to 1, $\bar{C}_{abs,\lambda}$ was not significantly larger than for smaller values of k_λ and was even smaller for some values of n_λ . This can be attributed to the fact that the monomers scattered more strongly for large values of k_λ , as also observed for aggregates with

more complex shapes [51]. Then, the incident EM wave was unable to penetrate the monomers where absorption takes place. In addition, for a given value of k_λ , increasing n_λ led to a slight increase in $\bar{C}_{abs,\lambda}$. This could be attributed to the fact that the larger index mismatch across the interface between the monomers and the surrounding medium caused EM waves entering the monomers to be confined in the monomers due to total internal reflection. For a given value of k_λ , $\bar{C}_{sca,\lambda}$ was observed to oscillate with increasing n_λ . These oscillations were caused by interferences and diffraction and are typical of dielectric scatterers [52,53]. The oscillations in $\bar{C}_{sca,\lambda}$ became increasingly damped as k_λ increased. For both Suspensions 1 and

2, the predictions of $\bar{C}_{abs,\lambda}$ and $\bar{C}_{sca,\lambda}$ by the equivalent coated sphere approximation increasingly deviated from the predictions by the T-matrix method with increasing values of n_λ and/or k_λ . This was also observed in our previous study [36]. However, it remains unclear how these discrepancies affect the values of effective optical properties of bispheres and quadrspheres retrieved by the inverse method based on the equivalent coated sphere model.

The average absorption $\bar{C}_{abs,\lambda}$ and scattering $\bar{C}_{sca,\lambda}$ cross-sections computed by the T-matrix method were used to retrieve $n_{\lambda,pred}$ and $k_{\lambda,pred}$ by approximating Suspensions 1 and 2 as suspensions of average projected area and volume-equivalent coated spheres with size distributions

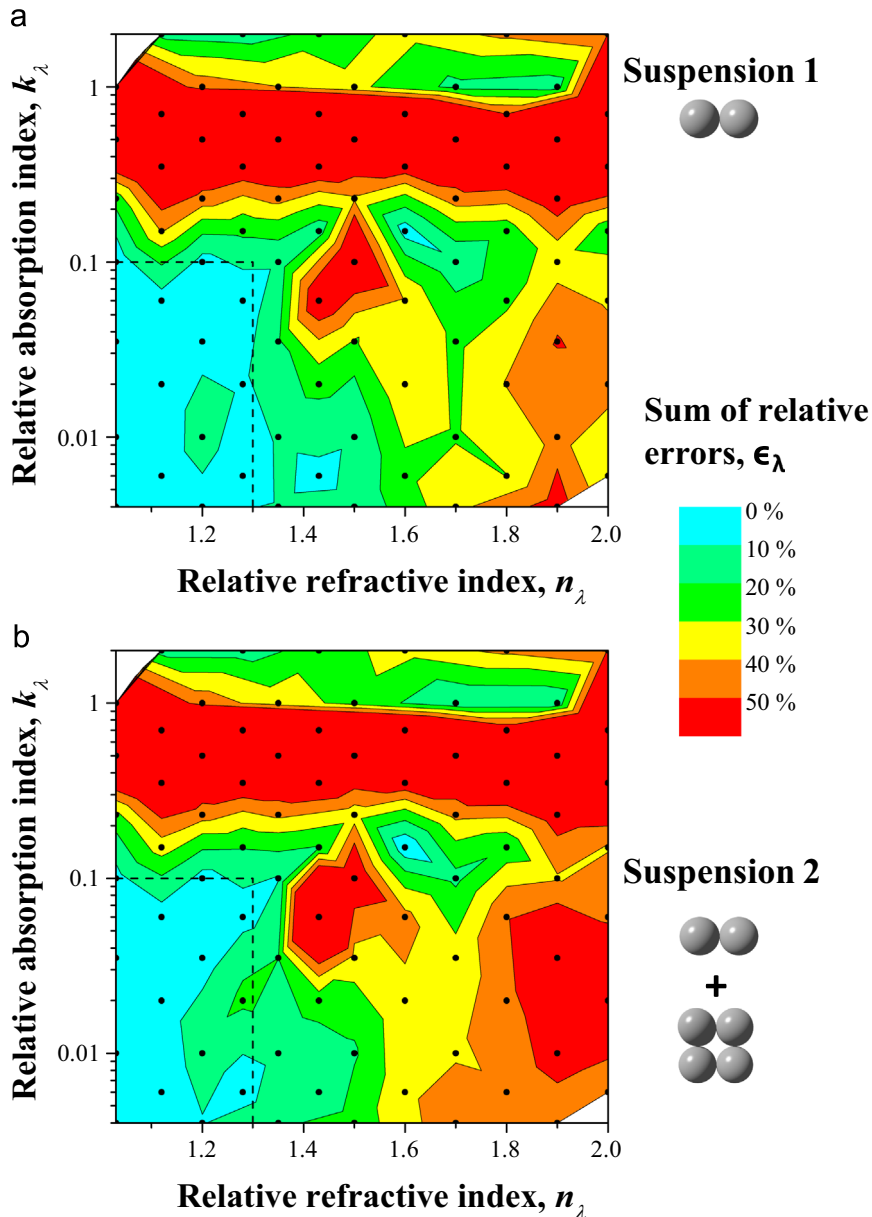


Fig. 7. Contour plots of the cumulative relative errors ϵ_λ between the input and retrieved refractive and absorption indices as a function of relative refractive n_λ and absorption k_λ indices of the monomers in (a) Suspensions 1 and (b) Suspension 2, respectively. The dots on the contour plots represent the location of the computed data points.

$f_{1,i}(r_{eq,i})$, $f_{1,o}(r_{eq,o})$ and $f_{2,i}(r_{eq,i})$, $f_{2,o}(r_{eq,o})$, respectively (Fig. 5). Figs. 7a and 7b show contour plots of the relative cumulative error ϵ_λ , defined by Eq. (13), as a function of the input relative refractive n_λ and absorption k_λ indices for Suspensions 1 and 2, respectively. In both cases, the contour plots showed similar trends. The error ϵ_λ was less than 10% for most of the domain defined by $1 \leq n_\lambda \leq 1.3$ and $0 \leq k_\lambda \leq 0.1$. More importantly, it was less than 1% in the region relevant to microalgae featuring $n_\lambda \leq 1.1$ and $\leq k_\lambda \leq 0.01$ [21,23,24,31]. In fact, in this range, for both suspensions 1 and 2, the maximum absolute error in n_λ and k_λ was 0.003 and 9×10^{-5} , respectively. This can be explained by the fact that, in this region, the coated sphere approximation gave excellent predictions of the T-matrix results, as illustrated in Fig. 6. Therefore, using the inverse method for photosynthetic microorganisms whose morphologies resemble that of bispheres and quadspheres, such as *Synechocystis* sp. is appropriate. In addition, the error ϵ_λ did not exceed 20% when n_λ was between 1.3 and 1.4 and k_λ was less than 0.1. In this range of n_λ and k_λ , corresponding to optically soft scatterers, the relative errors were considered acceptable and the inverse method was valid. Note that these results are consistent with

analysis of the forward problem indicating that approximations of bispheres and quadspheres by volume and average projected area equivalent coated spheres were valid for $n_\lambda \leq 1.2$ and $k_\lambda \leq 0.1$ for monomer size parameters χ_s ranging from 0.01 to 10 [36].

Finally, note that the complex index of refraction of cells in Suspensions 1 and 2 was also retrieved for an average *Synechocystis* cell with average radius determined from the size distribution and approximated as a single coated sphere. The error in the retrieved values of n_λ and k_λ increased only slightly compared with those retrieved using the actual size distribution. This suggests that the latter did not have a significant effect on the retrieved values of n_λ and k_λ .

5. Results and discussions

5.1. Radiation characteristics of *Synechocystis* sp.

5.1.1. Size distribution

Fig. 8a shows the histogram of the radius frequency distribution $f_{b,exp}(r_s)$ measured experimentally, with bin

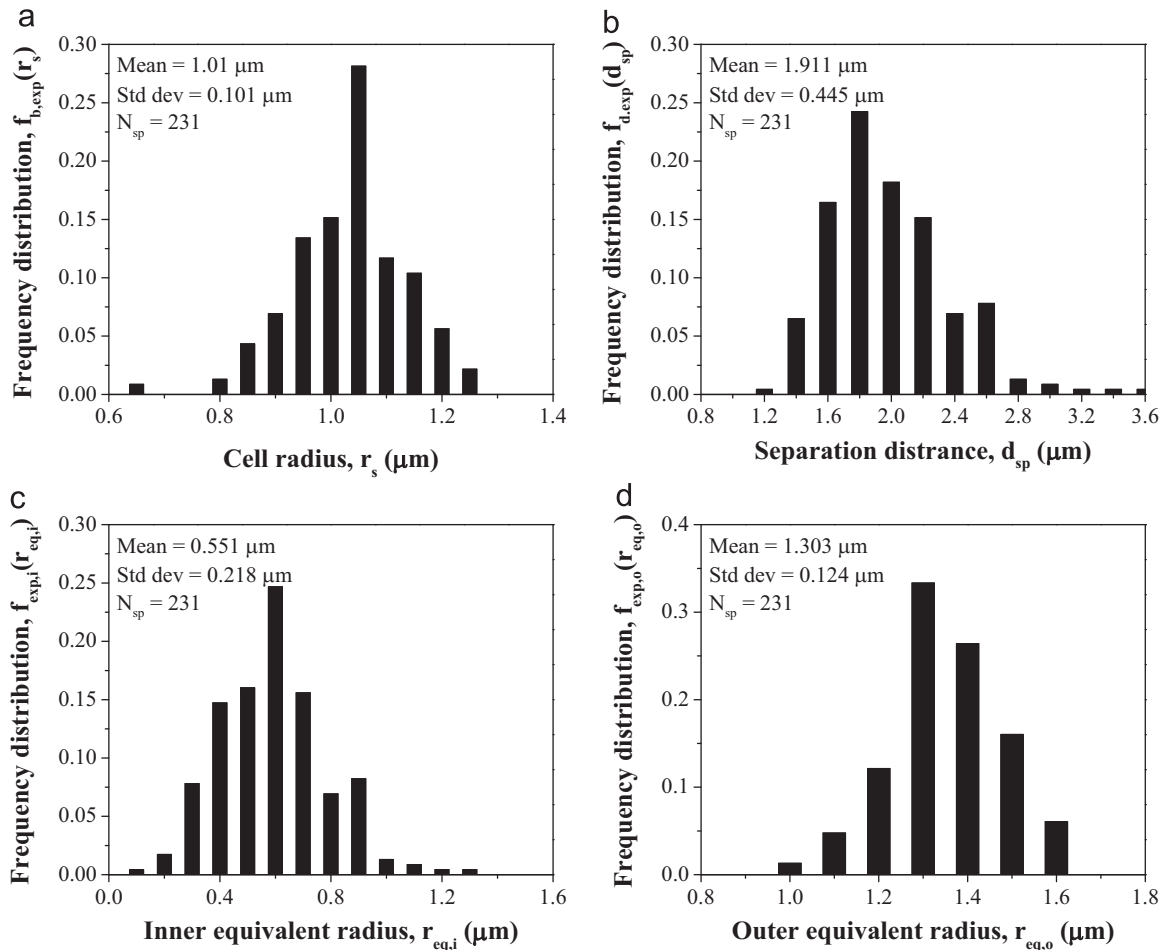


Fig. 8. Histograms of the measured *Synechocystis* sp. (a) radius distribution $f_{b,exp}(r_s)$, (b) separation distance distribution $f_{d,exp}(d_{sp})$ and of the equivalent coated sphere radii distributions (c) $f_{exp,i}(r_{eq,i})$ and (d) $f_{exp,o}(r_{eq,o})$.

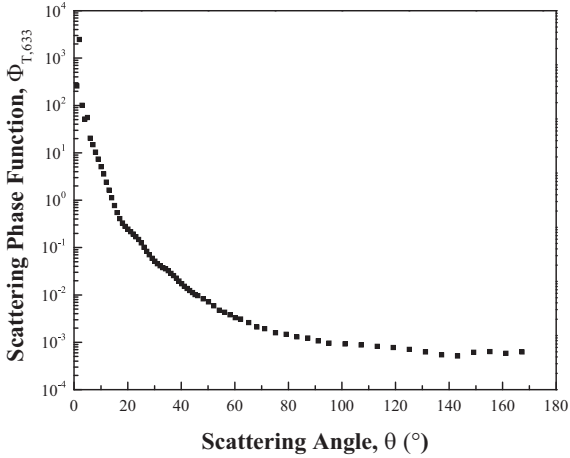


Fig. 9. Scattering phase function $\Phi_{T,633}(\theta)$ of *Synechocystis* sp. measured experimentally at 633 nm as a function of scattering angle θ using a polar nephelometer.

size of 0.05 μm , for *Synechocystis* sp. grown according to the experimental procedure previously described and featuring mean radius of 1.02 μm . For each of these cells, the radii $r_{s,1}$ and $r_{s,2}$ of the two lobes were found to fall within 20% of each other. Hence, treating the cells as bispheres with identical monomers of radius r_s taken as the average of $r_{s,1}$ and $r_{s,2}$ was reasonably accurate. Here, the monomer size parameter ranged from 6.3 to 18.8 over the PAR region. Fig. 6b shows the measured distribution $f_{d,exp}(d_{sp})$ for the distance d_{sp} separating the centers of the two lobes of *Synechocystis* cells treated as overlapping spheres (see Fig. 3a). Finally, Figs. 8c and 8d show histograms of the equivalent coated sphere radii distributions $f_{exp,i}(r_{eq,i})$ and $f_{exp,o}(r_{eq,o})$ converted from $f_{b,exp}(r_s)$ and $f_{d,exp}(d_{sp})$ using Eqs. (9) and (10).

5.1.2. Scattering phase function

Fig. 9 shows the scattering phase function $\Phi_{T,633}(\theta)$ of *Synechocystis* sp. measured at 633 nm. As expected,

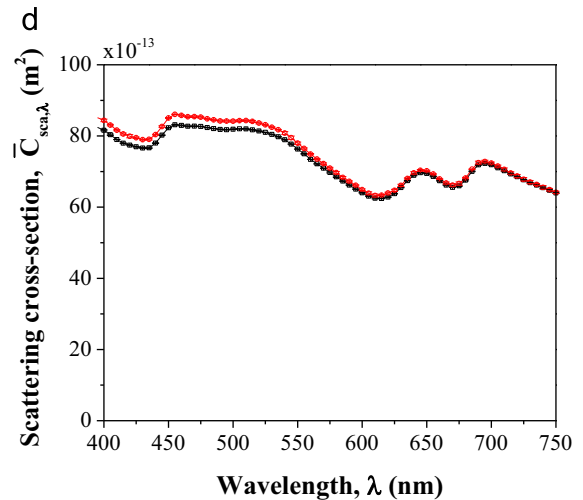
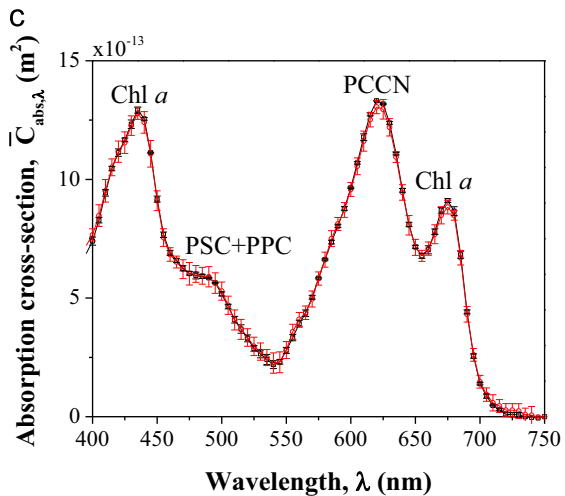
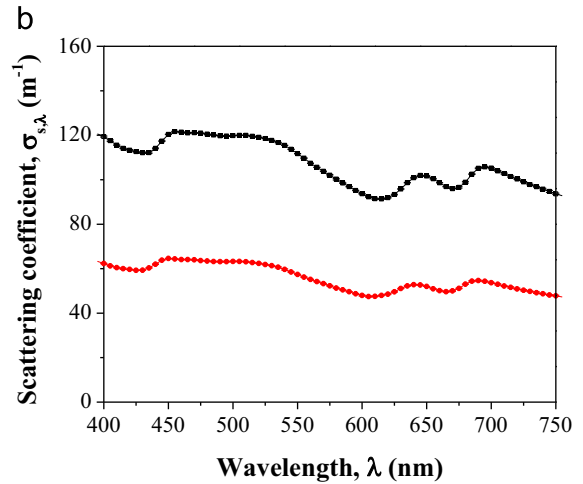
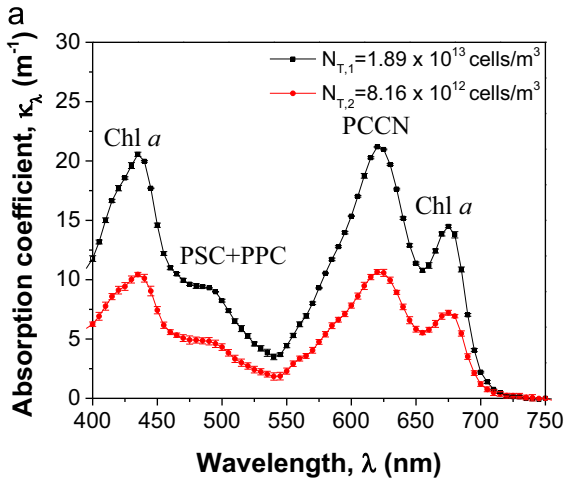


Fig. 10. Measured (a) absorption coefficient κ_λ , (b) scattering coefficient $\sigma_{s,\lambda}$, (c) average absorption cross-section $\bar{C}_{abs,\lambda} = \kappa_\lambda/N_T$, and (d) average scattering cross-section $\bar{C}_{scat,\lambda} = \sigma_{s,\lambda}/N_T$ of *Synechocystis* sp. as functions of wavelength λ from 400 to 750 nm for cell number densities $N_{T,1} = 1.89 \times 10^{13} \text{ cells/m}^3$ and $N_{T,2} = 8.16 \times 10^{12} \text{ cells/m}^3$.

scattering was strongly in the forward direction due to the large size parameters of the cells. In addition, the asymmetry factor g_{633} at wavelength of 633 nm was estimated to be 0.993.

5.1.3. Spectral absorption and scattering cross-sections

Figs. 10a and 10b, respectively, show the spectral absorption κ_λ and scattering $\sigma_{s,\lambda}$ coefficients measured in the spectral range from 400 to 750 nm for randomly oriented *Synechocystis* sp. collected after 6 days during the exponential growth phase for cell number densities $N_{T,1} = 1.89 \times 10^{13}$ cells/m³ and $N_{T,2} = 8.16 \times 10^{12}$ cells/m³. Each data point represents the arithmetic mean of κ_λ and $\sigma_{s,\lambda}$ measured three times for each cell number density while the error bars correspond to 95% confidence interval. It is evident that the sample with the largest cell number density $N_{T,1}$ had the largest absorption and scattering coefficients κ_λ and $\sigma_{s,\lambda}$.

Fig. 10c and d shows the average absorption $\bar{C}_{abs,\lambda}$ and scattering $\bar{C}_{sca,\lambda}$ cross-sections in the spectral range from 400 to 750 nm after normalizing κ_λ and $\sigma_{s,\lambda}$ [Fig. 10a and b] by their respective cell number density N_T , according to Eq. (4). Both datasets collapse on a single line confirming that single and independent scattering prevailed and that the absorption and scattering coefficients were directly proportional to the cell number density. Moreover, both the absorption coefficient κ_λ and the cross-section $\bar{C}_{abs,\lambda}$ of *Synechocystis* sp. featured (i) peaks at 435 and 676 nm corresponding to the absorption peaks of Chl *a* [11], (ii) a peak at 625 nm corresponding to PCCN [54], and (iii) a shoulder around 485 nm corresponding to absorption by PSC and PPC [11]. The scattering coefficient $\sigma_{s,\lambda}$ and the scattering cross-section $\bar{C}_{sca,\lambda}$ featured resonance peaks and dips around wavelengths corresponding to the absorption peaks.

5.2. Effective spectral optical properties of *Synechocystis* sp.

Synechocystis sp. cells were approximated as overlapping and homogeneous bispheres with some effective complex index of refraction. In addition, the spectral optical properties of *Synechocystis* sp. were retrieved using the inverse method illustrated in Fig. 4 from (i) the equivalent coated sphere radii distributions $f_{exp,i}(r_{eq,i})$ and $f_{exp,o}(r_{eq,o})$, (ii) the experimentally measured average absorption and scattering cross-sections $\bar{C}_{abs,\lambda}$ and $\bar{C}_{sca,\lambda}$, and (iii) the spectral refractive index of PBS reported as [55]

$$n_{m,\lambda} = 1.32711 + \frac{0.0026}{\lambda^2} + \frac{0.00005}{\lambda^4} \quad (14)$$

where the wavelength λ is expressed in μm .

Fig. 11 shows the average effective (a) refractive index $n_{s,\lambda}$ and (b) the effective absorption index $k_{s,\lambda}$ of *Synechocystis* sp. between 400 and 750 nm retrieved by the previously validated inverse method from six different experimental measurements of the absorption and scattering cross-sections. The error bars were estimated as two times the standard deviation of the retrieved values of $n_{s,\lambda}$ and $k_{s,\lambda}$ corresponding to 95% confidence interval. They were relatively small since the cross-section measurements featured small experimental uncertainty and the

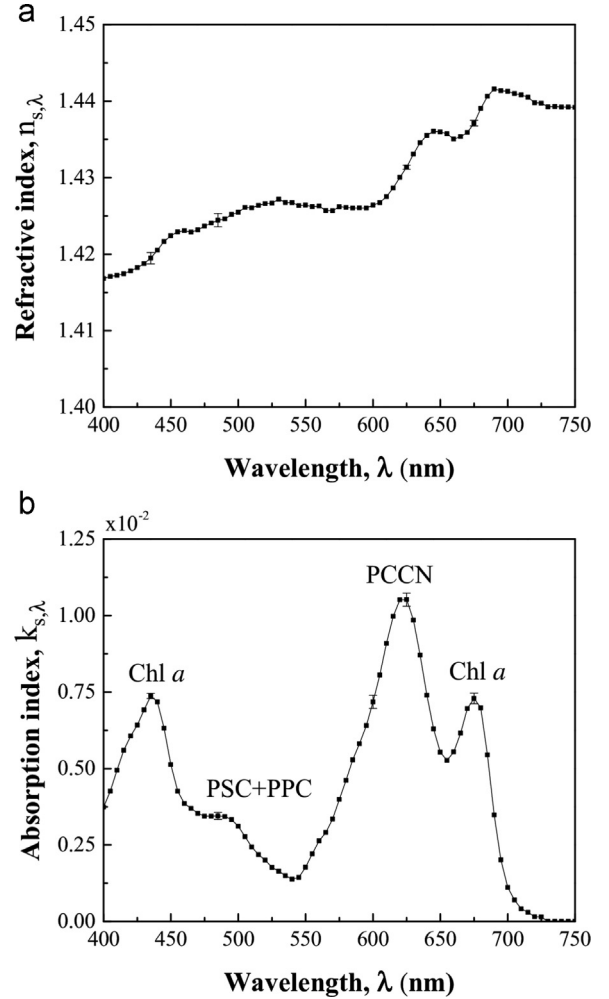


Fig. 11. Retrieved effective (a) refractive $n_{s,\lambda}$ and (b) absorption $k_{s,\lambda}$ indices of *Synechocystis* sp. as functions of wavelength λ from 400 to 750 nm using (i) the inverse method (Fig. 4) with (ii) distributions $f_{exp,i}(r_{eq,i})$ and $f_{exp,o}(r_{eq,o})$ (Fig. 8), and (iii) the cross-sections $\bar{C}_{abs,\lambda}$ and $\bar{C}_{sca,\lambda}$ (Fig. 10).

inverse method was able to accurately and repeatedly retrieve these effective optical properties. Although each pair $(n_{s,\lambda}, k_{s,\lambda})$ was retrieved independently for each individual wavelength, the inverse method resulted in $n_{s,\lambda}$ and $k_{s,\lambda}$ being continuous functions of wavelength. In addition, the absorption index $k_{s,\lambda}$ featured the same absorption peaks as those observed in κ_λ and $\bar{C}_{abs,\lambda}$ corresponding to Chl *a*, PCCN, and carotenoids, as previously discussed. The refractive index $n_{s,\lambda}$ featured resonance peaks and dips around wavelengths corresponding to the peaks in $k_{s,\lambda}$. The values of the retrieved absorption index $k_{s,\lambda}$ were consistent with those found for other photosynthetic microorganisms [21,31] and was such that $k_\lambda = k_{s,\lambda}/n_{m,\lambda}$ was less than 0.011. The retrieved refractive index $n_{s,\lambda}$ ranged between 1.4 and 1.44, corresponding to a relative refractive index $n_\lambda = n_{s,\lambda}/n_{m,\lambda}$ between 1.04 and 1.08. These values fell within the range of validity of the inverse method established earlier.

Moreover, $n_{s,\lambda}$ was slightly larger than those reported for cyanobacteria [21,56] and several hydrogen and lipid producing microalgae [31] ranging between 1.35 and 1.39. By contrast, it was smaller than the reported refractive index of coccolithophonds [28] ranging between 1.53 and 1.56. The difference in $n_{s,\lambda}$ can be attributed to the difference in cell composition among these microorganisms. For example, cells with higher water content would feature lower values of $n_{s,\lambda}$ while those with large lipid, protein, calcium, and/or carbohydrate contents would result in larger effective refractive index [28].

6. Conclusion

This paper reported, for the first time, the scattering phase function, the average spectral absorption and scattering cross-sections of randomly oriented dumbbell-shaped *Synechocystis* sp. measured experimentally from 400 to 750 nm during the exponential growth phase in F medium. Moreover, an inverse method was developed to retrieve the spectral refractive and absorption indices from the spectral absorption and scattering cross-sections. It was first validated using the average absorption and scattering cross-sections computed by the T-matrix method for two different suspensions of polydisperse randomly oriented bispheres and quadspheres. The inverse method was able to accurately retrieve the monomer complex index of refraction for relative refractive index less than 1.3 and relative absorption index less than 0.1. Then, it was used to retrieve spectral effective complex index of refraction of *Synechocystis* sp. cells approximated as equivalent coated spheres with identical average projected area and volume. Both the absorption cross-section and the absorption index featured distinct peaks corresponding to chlorophyll *a* and phycocyanin and a shoulder around 485 nm corresponding to carotenoids. These results can be used for predicting light distribution in photobioreactors cultivating *Synechocystis* sp. under optimal conditions. In addition, the inverse method can be applied to other optically soft absorbing and scattering particles of similar morphologies.

Acknowledgements

The authors would like to thank Prof. Brian Palenik, from the Scripps Institution of Oceanography of the University of California, San Diego, for providing the microorganisms. The computation for this study was performed on the Hoffman2 cluster hosted by the Academic Technology Services (ATS) at the University of California, Los Angeles.

References

- [1] Pulz O, Gross W. Valuable products from biotechnology of microalgae. *Appl Microbiol Biotechnol* 2004;65(6):635–48.
- [2] Richmond A. *Handbook of microalgal culture: biotechnology and applied phycology*. Oxford, UK: Blackwell Science Ltd; 2004.
- [3] Wang B, Li Y, Wu N, Lan CQ. CO₂ bio-mitigation using microalgae. *Appl Microbiol Biotechnol* 2008;79(5):707–18.
- [4] Chen CY, Yeh KL, Aisyah R, Lee DJ, Chang JS. Cultivation, photobioreactor design and harvesting of microalgae for biodiesel production: a critical review. *Bioresour Technol* 2011;102(1):71–81.
- [5] Nakajima Y, Ueda R. Improvement of photosynthesis in dense microalgal suspension by reduction of light harvesting pigments. *J Appl Phycol* 1997;9(6):503–10.
- [6] Kaneko T, Sato S, Kotani H, Tanaka A, Asamizu E, Nakamura Y, et al. Sequence analysis of the genome of the unicellular cyanobacterium *Synechocystis* sp. strain PCC6803 II. Sequence determination of the entire genome and assignment of potential protein-coding regions. *DNA Res* 1996;3(3):109–36.
- [7] Hihara Y, Sonoike K, Kanehisa M, Ikeuchi M. DNA microarray analysis of redox-responsive genes in the genome of the cyanobacterium *Synechocystis* sp. strain PCC 6803. *J Bacteriol* 2003;185(5):1719–25.
- [8] Lagarde D, Beuf L, Vermaas W. Increased production of zeaxanthin and other pigments by application of genetic engineering techniques to *Synechocystis* sp. strain PCC 6803. *Appl Environ Microbiol* 2000;66(1):64–72.
- [9] Vega-Palas MA, Madueño F, Herrero A, Flores E. Identification and cloning of a regulatory gene for nitrogen assimilation in the cyanobacterium *Synechocystis* sp. strain PCC 7942. *J Bacteriol* 1990;172(2):643–7.
- [10] Scott M, McCollum C, Vasil'ev S, Crozier C, Espie GS, Krol M, et al. Mechanism of the down regulation of photosynthesis by blue light in the cyanobacterium *Synechocystis* sp. PCC 6803. *Biochemistry* 2006;45(29):8952–8.
- [11] Bidigare R, Ondrusek M, Morrow J, Kiefer D. In vivo, absorption properties of algal pigments. In: Proceedings of the society of photo-optical instrumentation, vol. 1302, Ocean optics X; 1990. p. 290–301.
- [12] Pinho MG, Kjos M, Veening JW. How to get (a) round: mechanisms controlling growth and division of coccoid bacteria. *Nat Rev Microbiol* 2013;11(9):601–14.
- [13] Grobbelaar JU. Physiological and technological considerations for optimising mass algal cultures. *J Appl Phycol* 2000;12(3–5):201–6.
- [14] Eriksen NT. The technology of microalgal culturing. *Biotechnol Lett* 2008;30(9):1525–36.
- [15] Pruvost J, Cornet J-F. Knowledge models for engineering and optimization of photobioreactors. In: Posten C, Walter C, editors. *Microalgal biotechnology*. Berlin, Germany: Walter De Gruyter; 2012. p. 181–224 (Chapter 10).
- [16] Pruvost J, Cornet J-F, Pilon L. Large scale production of algal biomass: photobioreactors. In: Chisti Y, Bux F, editors. *Algae biotechnology: products and processes*. UK: Springer; 2015.
- [17] Olivieri G, Salatino P, Marzocchella A. Advances in photobioreactors for intensive microalgal production: configurations, operating strategies and applications. *J Chem Technol Biotechnol* 2014;89(20):178–95.
- [18] Pilon L, Berberoğlu H, Kandilian R. Radiation transfer in photobiological carbon dioxide fixation and fuel production by microalgae. *J Quant Spectrosc Radiat Transf* 2011;112(17):2639–60.
- [19] Jonasz M, Fournier G. *Light scattering by particles in water: theoretical and experimental foundations*. San Diego, CA: Academic Press; 2007.
- [20] Berberoğlu H, Pilon L. Experimental measurement of the radiation characteristics of *Anabaena variabilis* ATCC 29413-U and *Rhodospira rubra* ATCC 49419. *Int J Hydrogen Energy* 2007;32(18):4772–85.
- [21] Heng RL, Lee E, Pilon L. Radiation characteristics and optical properties of filamentous cyanobacterium *Anabaena cylindrica*. *J Opt Soc Am A* 2014;31(4):836–45.
- [22] Berberoğlu H, Pilon L, Melis A. Radiation characteristics of *Chlamydomonas reinhardtii* CC125 and its truncated chlorophyll antenna transformants *ta1*, *taX* and *ta1-CW+*. *Int J Hydrogen Energy* 2008;33(22):6467–83.
- [23] Kandilian R, Lee E, Pilon L. Radiation and optical properties of *Nannochloropsis oculata* grown under different irradiances and spectra. *Bioresour Technol* 2013;137:63–73.
- [24] Morel A, Bricaud A. Inherent optical properties of algal cells including picoplankton: theoretical and experimental results. *Can Bull Fish Aquat Sci* 1986;214:521–59.
- [25] Stramski D, Rosenberg G, Legendre L. Photosynthetic and optical properties of the marine chlorophyte *Dunaliella tertiolecta* grown under fluctuating light caused by surface-wave focusing. *Mar Biol* 1993;115(3):363–72.
- [26] Bricaud A, Morel A. Light attenuation and scattering by phytoplanktonic cells: a theoretical modeling. *Appl Opt* 1986;25(4):571–80.

- [27] Stramski D, Morel A. Optical properties of photosynthetic picoplankton in different physiological states as affected by growth irradiance. *Deep Sea Res Part A. Oceanogr Res Pap* 1990;37(2): 245–66.
- [28] Aas E. Refractive index of phytoplankton derived from its metabolite composition. *J Plankton Res* 1996;18(12):2223–49.
- [29] Pottier L, Pruvost J, Deremetz J, Cornet J-F, Legrand J, Dussap C-G. A fully predictive model for one-dimensional light attenuation by *Chlamydomonas reinhardtii* in a torus photobioreactor. *Biotechnol Bioeng* 2005;91(5):569–82.
- [30] Gordon HR. Light scattering and absorption by randomly-oriented cylinders: dependence on aspect ratio for refractive indices applicable for marine particles. *Opt Express* 2011;19(5):4673–91.
- [31] Lee E, Heng RL, Pilon L. Spectral optical properties of selected photosynthetic microalgae producing biofuels. *J Quant Spectrosc Radiative Transf* 2013;114:122–35.
- [32] Mie G. Beiträge zur Optik trüber Medien, speziell kolloidaler Metallungen. *Ann Phys* 1908;25(30):377–445.
- [33] van de Hulst HC. Light scattering by small particles. Mineola, NY: Courier Dover Publications; 2012.
- [34] Mackowski DW, Mishchenko MI. A multiple sphere T-matrix Fortran code for use on parallel computer clusters. *J Quant Spectrosc Radiat Transf* 2011;112(13):2182–92.
- [35] Quirantes A, Bernard S. Light scattering by marine algae: two-layer spherical and nonspherical models. *J Quant Spectrosc Radiat Transf* 2004;89(1):311–21.
- [36] Heng RL, Sy KC, Pilon L. Absorption and scattering by bispheres, quadrspheres, and circular rings of spheres and their equivalent coated spheres. *J Opt Soc Am A* 2015;32(1):46–60.
- [37] Kandilian R, Heng RL, Pilon L. Absorption and scattering by fractal aggregates and by their equivalent coated spheres. *J Quant Spectrosc Radiat Transf* 2015;151:310–26.
- [38] Aden AL, Kerker M. Scattering of electromagnetic waves from two concentric spheres. *J Appl Phys* 1951;22(10):1242–6.
- [39] Lee SC. Radiative transfer through a fibrous medium: allowance for fiber orientation. *J Quant Spectrosc Radiat Transf* 1986;36:253–63.
- [40] Lee SC. Radiation heat-transfer model for fibers oriented parallel to diffuse boundaries. *J Thermophys Heat Transf* 1988;2:303–8.
- [41] Lee E, Pilon L. Absorption and scattering by long and randomly oriented linear chains of spheres. *J Opt Soc Am A* 2013;30(9): 1892–900.
- [42] Dauchet J. Analyse Radiative des Photobioréacteurs [Ph.D. thesis]. France: Université Blaise Pascal, Clermont Ferrand II; 2012.
- [43] Quirantes A, Bernard S. Light-scattering methods for modelling algal particles as a collection of coated and/or nonspherical scatterers. *J Quant Spectrosc Radiat Transf* 2006;100(1):315–24.
- [44] Charbonneau P, Knapp B. A User's guide to PIKAIA 1.0. Technical report. NCAR technical note 418+IA. National Center for Atmospheric Research; 1995.
- [45] Kerker M. The scattering of light, and other electromagnetic radiation. New York, NY: Academic Press; 1969.
- [46] Bohren CF, Huffman DR. Absorption and scattering of light by small particles. New York, NY: John Wiley & Sons; 1998.
- [47] Guillard RRL, Ryther JH. Studies of marine planktonic diatoms: I. *Cyclotella nana* Hustedt, and *Detonula confervacea* (Cleve) Gran. *Can J Microbiol* 1962;8(2):229–39.
- [48] Heng RL, Pilon L. Time-dependent radiation characteristics of *Nannochloropsis oculata* during batch culture. *J Quant Spectrosc Radiat Transf* 2014;144:154–63.
- [49] Weisstein EW. Sphere–sphere intersection. In: Eric Weisstein's world of mathematics (<http://mathworld.wolfram.com/>); 2002.
- [50] Brown DJ, Vickers GT. The use of projected area distribution functions in particle shape measurement. *Powder Technol* 1998;98(3): 250–7.
- [51] Zubko E, Kimura H, Shkuratov Y, Muinonen K, Yamamoto T, Okamoto H, et al. Effect of absorption on light scattering by agglomerated debris particles. *J Quant Spectrosc Radiat Transf* 2009;110 (14–16):1741–9.
- [52] Modest M. Radiative heat transfer. 3rd edition Oxford, UK: Elsevier; 2013.
- [53] Jones AR. Light scattering for particle characterization. *Prog Energy Combust Sci* 1999;25(1):1–53.
- [54] Su X, Fraenkel PG, Bogorad L. Excitation energy transfer from phycocyanin to chlorophyll in an apcA-defective mutant of *Synechocystis* sp. PCC 6803. *J Biol Chem* 1992;267(32):22944–50.
- [55] Zhernovaya O, Sydoruk O, Tuchin V, Douplik A. The refractive index of human hemoglobin in the visible range. *Phys Med Biol* 2011;56: 4013–21.
- [56] Bricaud A, Bédhomme AL, Morel A. Optical properties of diverse phytoplanktonic species: experimental results and theoretical interpretation. *J Plankton Res* 1988;10(5):851–73.